Nanoscale Horizons

ROYAL SOCIETY OF CHEMISTRY

COMMUNICATION

View Article Online
View Journal | View Issue

Cite this: *Nanoscale Horiz.*, 2025, **10**, 1084

Received 30th January 2025,
Accepted 15th April 2025

DOI: 10.1039/d5nh00049a

rsc.li/nanoscale-horizons

Multifunctional $Ti_3C_2T_x$-alginate foams for energy harvesting and fire warning†

Bernd Wicklein, *[a] Hyunjoon Yoo,[b] Geetha Valurouthu, [c] Ji-Seok Kim,[b] Mannan Khan,[b] Manmatha Mahato,[b] Federico Carosio, [d] Yury Gogotsi [c] and Il-Kwon Oh *[b]

Foams that combine seemingly opposite properties, such as high thermal insulation and electrical conductivity, are highly sought after for modern-day advanced applications. However, achieving a balance of these properties necessitates careful tuning of material compositions. Here, we prepared ice-templated $Ti_3C_2T_x$-alginate composite foams and investigated the role of $Ti_3C_2T_x$ MXene in triboelectric energy production, thermal insulation, and flame retardancy. Our results show that adding 5 wt% $Ti_3C_2T_x$ enhances the triboelectric output of 6 mm thick foams (380 V, 7.7 μA, 43 mW m^{-2}) by 110%. Despite incorporating electrically conducting $Ti_3C_2T_x$, these macroporous composite foams have a thermal conductivity of only 62 mW m^{-1} K^{-1}, while they also show flame-retardant properties, exhibiting self-extinguishing behavior. Finally, we demonstrate these composite foams for constructing smart fire alarm systems as they respond to small changes in electrical resistance induced by fire. Our findings prove that $Ti_3C_2T_x$ is a versatile filler for biopolymer foams, introducing complementary functionalities that can be exploited in energy and safety applications.

New concepts

Porosity is essential for thermal insulation but also plays a role in triboelectric nanoenergy generation. We demonstrate how porosity helps to improve the triboelectric output, thermal insulation, and flame retardancy of MXene composite materials. While there are limited reports on thin, porous films used in triboelectric nanogenerators (TENGs), a more systematic study examining how the thickness of porous materials affects triboelectric performance is still lacking. Given this gap, the significance of the present study is the finding that incorporating $Ti_3C_2T_x$ in alginate allows the use of millimeter-thick foams in TENG devices, which would not be possible otherwise. The increased thickness enhances significantly the triboelectric output while also providing thermal insulation. The composite foam panels have a very low thermal conductivity and a radiation cooling effect. Additionally, these composite foams display flame-retardant properties. Our findings reveal that the electrical resistance of the foams decreased upon fire exposure, which triggers a fast-response fire alarm system capability in just 2 seconds. These results offer a deeper understanding of the versatility of MXene biopolymer foams, leading to a new generation of smart insulation materials generating not only electricity but also serving as effective flame-retardants and fire alarm systems.

Introduction

Foams are an important class of materials utilized in various applications, including energy, aerospace, construction, biomedicine, and environmental remediation.[1–5] Composition, texture, and porosity are crucial parameters that modulate their functional and structural properties. For instance, incorporating functional inorganic fillers in a polymer matrix increases charge accumulation, roughness, and flame retardancy. On the other hand, ice-templating can control the pore structure, improving thermal transport and mechanical strength.[6–8] Interestingly, it has also been shown that porosity plays a role in triboelectric energy generation by increasing the contact and friction surface areas and the number of charge traps.[9,10] Triboelectric nanogenerators (TENGs) produce electricity using a combination of contact electrification and electrostatic induction.[11] The materials used in TENGs are typically polymer-based and designed to be both thin and dense. This is because the output of a TENG decreases with the increasing thickness of the dielectric film, as described by the distance-dependent electric field (DDEF) model[12] and supported by experimental studies.[12,13] According to the DDEF model, integration of eqn (1),

$$E_{\mathrm{Tot}} = \frac{\sigma}{\pi\varepsilon_0}[f(d) - f(d-x)] \quad (1)$$

[a] *Materials Science Institute of Madrid (ICMM), Consejo Superior de Investigaciones Científicas (CSIC), 28049 Madrid, Spain. E-mail: bernd@icmm.csic.es*
[b] *Department of Mechanical Engineering, Korea Advanced Institute of Science and Technology (KAIST), Daejeon, 34141, Republic of Korea. E-mail: ikoh@kaist.ac.kr*
[c] *Department of Materials Science & Engineering, and A. J. Drexel Nanomaterials Institute, Drexel University, Philadelphia, Pennsylvania, 19104, USA*
[d] *Dipartimento di Scienza Applicata e Tecnologia, Politecnico di Torino – Alessandria campus, Viale T. Michel 5, 15121 Alessandria, Italy*

† Electronic supplementary information (ESI) available. See DOI: https://doi.org/10.1039/d5nh00049a

where E_{Tot} is the overall electrical field resulting from positive and negative tribo-charges, σ represents the surface charge density, ε_0 denotes the permittivity of free space, and f is a function of the thickness d of the dielectric film and the variable separation x between the charged surfaces, yields the thickness- and geometry-dependent TENG output. This model also suggests that the output increases with the contact area. Because more charge can be accumulated on the external and internal contact areas compared to dense films (of the same thickness), the electrical output of porous TENGs increases. Consequently, various porous materials have been investigated as TENG components, such as polyurethane foams,[14] polydimethylsiloxane (PDMS) cryogels,[15] polyimide aerogels,[16] and polyaniline sponges.[17] In all these cases, both the current and voltage increased with the increase in porosity, indicating that not only does a larger external contact surface enhance performance, but the friction of the internal surfaces also contributes to improved performance. A common feature of these examples is that the aerogels were compressed to relatively thin sheets (on the order of tens of microns) before being employed as TENG components to help maintain a small thickness without compromising output. In contrast, incorporating dielectric fillers like $BaTiO_3$ allows the thickness of a chitosan aerogel TENG to be increased to around 1 mm while still achieving acceptable performance.[9] The proposed mechanism is that the dielectric particles become polarized by the electric field generated from the external surface charge. This polarization extends the electric field deeper into the material, enabling strong electrostatic induction in the backside electrode connected to the external circuit.

Yet, a more systematic study examining how the thickness of porous material affects triboelectric performance is still lacking. Additionally, the complementary properties of multifunctional foams resulting from their porosity remain largely unexplored. For instance, foams are excellent thermal insulators, and this property could be combined with triboelectric energy generation. However, these foams must be thick enough for effective insulation without compromising their triboelectric performance. Recently, we showed alginate, a renewable biopolymer matrix, which, when combined with $Ti_3C_2T_x$, exhibited high triboelectric output as dense films.[18] In this work, we prepared foams from polymer-$Ti_3C_2T_x$ composites with a thickness of several mm and investigated their triboelectric and thermal transport properties. $Ti_3C_2T_x$ belongs to a family of 2-dimensional (2D) transition metal carbides/nitrides/carbonitrides known as MXenes, where T_x denotes surface functionalities (*e.g.*, F, O, and OH).[19] MXenes are particularly interesting due to their electrical, thermal, optical, and catalytic properties including triboelectricity.[20] Recently, these materials have been incorporated into synthetic polymer foams and aerogels, providing the composites with electrical conductivity and excellent electromagnetic interference shielding capabilities.[21–23] Additionally, MXenes have been reported to have infrared (IR) reflection properties and low IR emissivity, which help block thermal dissipation[24–26] and are useful for thermal insulation applications.[27] MXenes also display flame retardant behavior by creating physical barriers and catalyzing carbonization processes in polymer composites, thereby improving fire safety.[28,29] Taking advantage of the variable electrical conductivity of MXenes, MXene-based fire alarm systems have also been proposed.[28]

In this work, we combined various properties of MXenes and foams to construct multifunctional macroporous $Ti_3C_2T_x$-alginate composite panels employing the freeze-casting method. We chose alginate because it shows triboelectric behavior, has flame retardant properties, is biodegradable and forms stable, aqueous colloidal dispersions with fillers, which are ideal for processing. Our results demonstrate that the addition of 5 wt% $Ti_3C_2T_x$ enables efficient triboelectric energy harvesting, even with foam panels that are 6 mm in thickness. IR imaging and transient thermal conductivity measurements reveal their good insulation properties. We employed cone calorimetry, thermogravimetric analysis, X-ray diffraction, and scanning electron microscopy to investigate the flame-retardant behavior of the composite. Additionally, we demonstrated a fire safety system capable of triggering an alarm signal within 2 seconds, activated by the composite's reduced electrical resistance upon exposure to fire.

Yury Gogotsi

In our first paper in Nanoscale Horizons, published in 2016, we reported on controlling the properties of 2D carbides (MXenes) by changing their compositions. Since then, over twenty thousand papers on carbide and nitride MXenes have been published, and thousands of MXene patents have been filed worldwide. We are glad to continue submitting some of our most important MXene research to Nanoscale Horizons, which publishes high-quality, innovative articles reporting conceptual advances in nanoscience and nanomaterials. Congratulations and best wishes to the Nanoscale Horizons on the 10th anniversary!

Materials & methods

Materials

Ti, TiC, Al, HCl, HF, LiCl, and alginic acid (sodium salt from brown algae, low viscosity grade) were procured from Sigma-Aldrich. Mixed cellulose ester (MCE, VSWP) films were purchased from Millipore-Sigma.

Materials synthesis

$Ti_3C_2T_x$ was prepared by HCl/HF etching of the corresponding Ti_3AlC_2 MAX phase according to protocols reported previously.[30] In brief, precursor powders of TiC (Alfa Aesar, 99.5%, 2 μm powder), Ti (Thermo Scientific, 99.5%, 325 mesh),

and Al (Thermo Scientific, 99.5%, 325 mesh) were combined in stoichiometric proportions of 2:1.25:2.2 (50 g batch size) and sintered at 1380 °C for 2 h under a continuous argon gas flow, with a heating and cooling rate of 3 °C min^{-1}. Next, 1 g of ground Ti_3AlC_2 (particle size <38 μm) was etched using 2 ml of HF (Thermo Scientific, 48–51% w/w, ACS reagent), 12 ml of HCl (Fisher Scientific, 37% w/w), and 6 ml of deionized water (DW) for 24 h at 35 °C under stirring. The mixture was centrifuged (3500 rpm, 5 min), and the sedimented solid was repeatedly washed until the pH value of the supernatant was greater than 6. The collected solid was delaminated in 20 mL of LiCl (Thermo Scientific, 99%, anhydrous) solution (50 mg ml^{-1}) and stirred for 24 h at 35 °C. The solid was recovered by centrifugation (3500 rpm, 10 min) and washed repeatedly until the supernatant turned dark, which indicates effective delamination. At this point, the supernatant was collected, and the remaining sediment was repeatedly resuspended in DW and shaken until all $Ti_3C_2T_x$ was collected as a colloidal suspension with a final concentration of 8 mg ml^{-1} (concentration determined gravimetrically). The suspensions were stored at 4 °C and processed within a month.

Foam preparation

Alginate was dissolved in DW at 6 mg ml^{-1} and homogenized in a planetary mixer (Thinky Mixer AR100) at 2200 rpm for 40 min. Then, aliquots of $Ti_3C_2T_x$ colloidal suspension were added to attain 1, 2, and 5 wt% of $Ti_3C_2T_x$ with respect to the polymer content. The mixtures (6 to 16 ml depending on the mold size) were again homogenized (20 min at 2200 rpm) and then poured into rectangular acrylate molds before freezing at −20 °C. The frozen samples were lyophilized in an Eyela FD-1000 Freeze dryer, resulting in porous foams. For comparison, solvent-cast alginate films were prepared from 1 mg ml^{-1} alginate solutions and dried at 40 °C, while $Ti_3C_2T_x$ films were obtained by vacuum filtration.

Characterization

The morphology of the foams was imaged using a JEOL JSM-IT800 scanning electron microscopy (SEM) after 3.4 nm osmium sputtering of the sample surface. Energy-dispersive X-ray spectroscopy (EDX) maps were acquired on a FEI NOVA Nano SEM 230. Apparent densities were calculated by weighing the foams (one per composition) and measuring their volumes with a caliper. Electrical measurements were carried out with a Keithley DMM75100 digital multimeter.

The mechanical properties were evaluated in compressive stress–strain tests using a MicroTester (INSTRON 5848, INSTRON) equipped with a 100 N load cell. Four samples per composition with a size of 13 × 13 × 6 mm^3 size were tested.

Thermal transport properties of the foams were analyzed using a Hot Disk TPS 2500 S instrument (Hot-disk AB) applying an output power of 10 mW in transient mode and employing a 3.2 mm Ni wire sensor. The data were obtained from five independent measurements per composition on two individual samples. Thermographic images of foams placed on a hot plate set at 50 °C were taken with an infrared thermal camera (FLIR A35SC).

Triboelectric voltage (DPO 3052, Tektronix) and short-circuit current (6514, Keithley) of the foam TENG were recorded during contact-separation with a tribonegative MCE film at a frequency of 10 Hz and an impact force of 8 N. These oscillations were generated by a mechanical shaker (S510575, TIRA) connected to a power amplifier (Type BAA120) and a function generator (AFG3022, Tektronix). The foams and MCE film were attached to adhesive aluminum tape to connect them to the external circuit. These measurements were conducted at 22 °C and 20–23% relative humidity (RH). The provided output curves represent the triboelectric behavior of several individual samples per composition and were acquired over at least 2 minutes of mechanical stimulation.

The thermal stability was evaluated using the Thermogravimetric Analysis (TGA, TGA5500, TA analysis). The samples were placed in platinum pans and heated from 50 to 800 °C at 10 °C min^{-1}. The measurements were performed in both N_2 and technical air atmospheres. Forced combustion tests were performed on an oxygen consumption cone calorimeter (Noselab, Milan, Italy). Cylindrical samples (diameter = 25 mm, height = 8 mm) were exposed to a heat flux of 35 kW m^{-2} in a horizontal configuration for up to 500 s. Two samples from each formulation were tested. The ignition and heat release rate (HRR, kW m^{-2}) were evaluated. Samples were conditioned in a climatic chamber at 23.0 ± 0.1 °C and 50.0 ± 0.1% RH for 48 h before testing. The morphology of the post-combustion residues collected after cone calorimetry tests was imaged by a scanning electron microscopy (Zeiss Evo 15) operating at 20 kV, equipped with an energy-dispersive X-ray spectroscopy probe (EDX, ULTIM MAX 40) to perform elemental analyses. Samples were positioned on conductive tape and sputtered with gold before measurements. X-ray diffraction (XRD) pattern of the post-combustion residues collected after cone calorimetry tests were performed with a PANalytical X'Pert Pro with a Philips PW3040/60 X-ray generator and a PIXcell 1d detector. Diffractograms were acquired in the 2θ range of 10–60° with a step size of 0.026° 2θ and a nominal time of 100 s per step.

Results and discussion

Composite foam preparation and characterization

$Ti_3C_2T_x$-alginate composite foams were produced by freezing aqueous dispersions containing 1–5 wt% $Ti_3C_2T_x$ with respect to the polymer content (60 mg ml^{-1}). The $Ti_3C_2T_x$ loading was limited to 5 wt%, because it was previously observed that the triboelectric properties deteriorate at higher loading, possibly related to filler aggregation.[18] After homogenization using planetary mixing, the dispersions were poured into molds and frozen at −20 °C (Fig. 1(a)). The subsequent lyophilization of the frozen blocks rendered rectangular foams of 3 × 3 and 5 × 5 cm^2, with a thickness ranging from 3 to 6 mm, depending on the chosen mold. The foams have a lamellar macropore structure, as seen from surface scanning electron microscopy (SEM) images (Fig. 1(b)). These composite foams were assembled with a mixed cellulose ester (MCE) film to build a

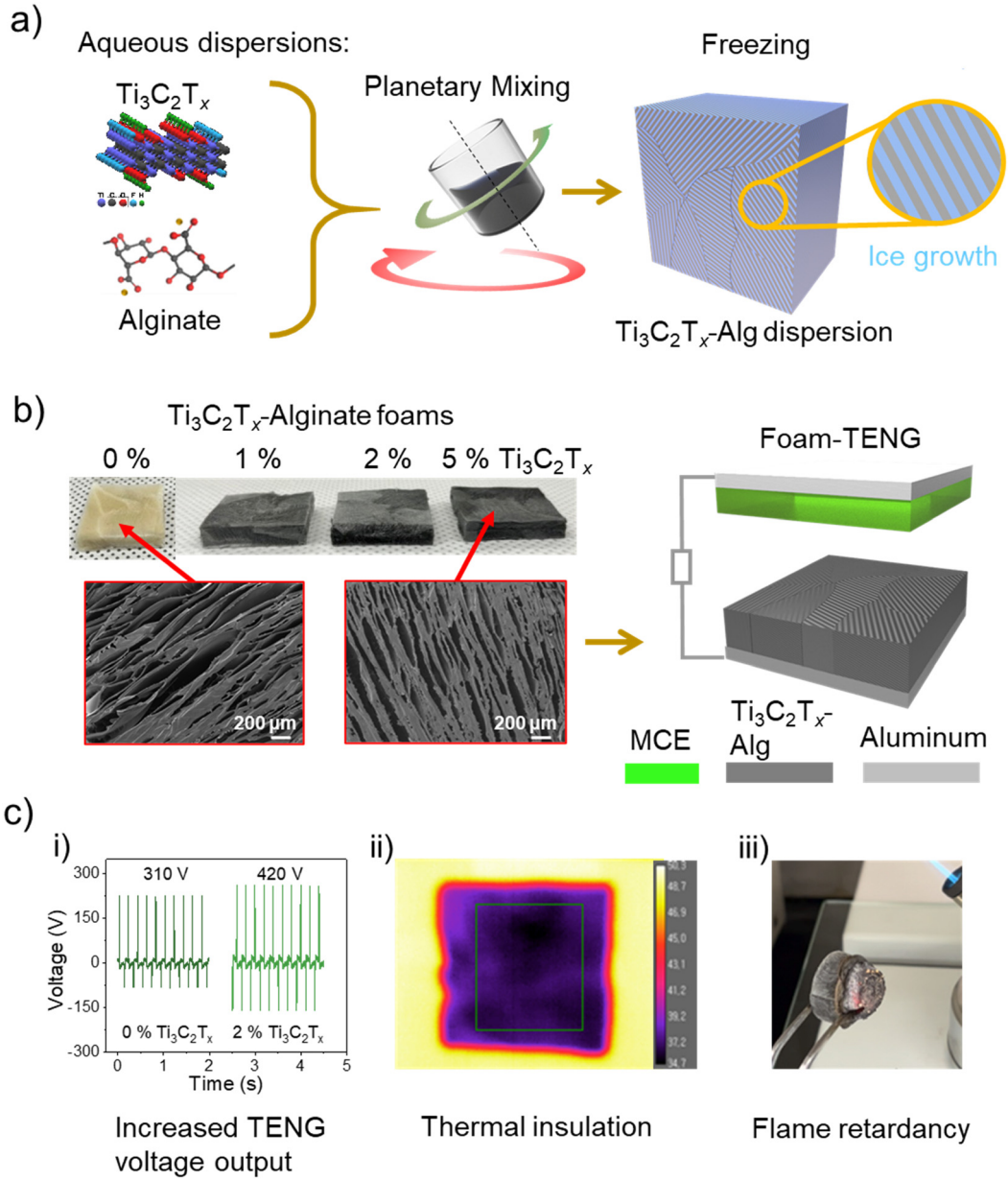

Fig. 1 Study overview from foam preparation to demonstrating multifunctional properties. Illustration of the mixing and lyophilization of the $Ti_3C_2T_x$-alginate composite foams (a). Digital photographs of lyophilized foams, with inset surface SEM images and an illustration of the foam-TENG setup (b). Triboelectric voltage curves of a composite foam (ci), thermographic camera image of a 5%$Ti_3C_2T_x$-alginate composite foam on a 50 °C hotplate (cii) and a 5%$Ti_3C_2T_x$-alginate composite foam after a flammability test (ciii).

triboelectric nanogenerator (TENG). The output of the foam-TENG increased with higher $Ti_3C_2T_x$ content (Fig. 1(c)-i). Additionally, the composite foams demonstrated high thermal insulation, self-extinguishing, and flame-retardant behavior (Fig. 1(c)-ii, iii).

The lamellar macropore structure of the 5% $Ti_3C_2T_x$ composite and alginate foams (Fig. 1(b) and 2(a), (b)) results from the anisotropic growth of ice crystals. The pore size (interlamellar spacing) ranges from 20 to 200 µm, while the thickness of the pore walls is around 2–5 µm. These characteristics did not change significantly with the $Ti_3C_2T_x$ content as seen from the 2% $Ti_3C_2T_x$ composite in Fig. S1a (ESI†). The $Ti_3C_2T_x$-alginate foams (2 and 5%) showed long protrusions like a bridge connecting the lamellas on the inner pore walls (Fig. 2(b), inset and Fig. S1b, ESI†), contrasting with the smoother surfaces of the pure alginate foam. Such bridges between lamellae form when the moving solidification front entraps suspended particles.[8,31] This can happen when the large MXene flakes (*ca.* 5 µm, Fig. S2, ESI†) are not rejected in time from the advancing ice front due to viscosity, particle orientation, interparticle forces, and interfacial energies.[23,31] The addition of $Ti_3C_2T_x$ flakes increased the surface roughness of the lamellae (Fig. 2(c)), consistent with the morphology of solvent-cast MXene-alginate films observed previously.[18] In contrast, plain

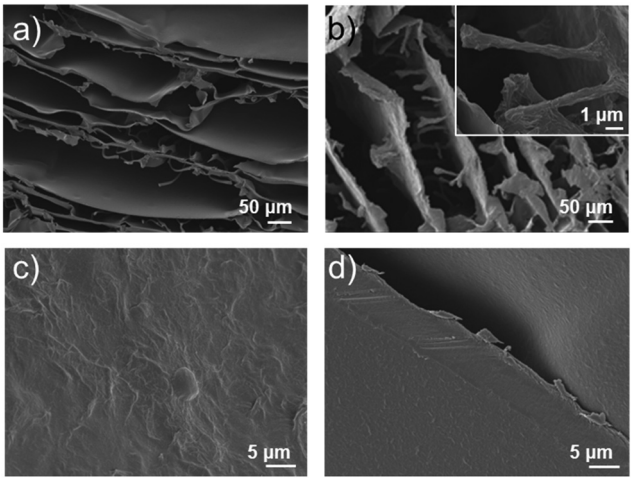

Fig. 2 Morphology of the foams. SEM cross-sectional images of an alginate (a) and 5%$Ti_3C_2T_x$-alginate foam; inset shows details at higher magnification (b). Images of the foam wall surfaces of 5%$Ti_3C_2T_x$-alginate and alginate foams (c), (d).

alginate produces smoother surfaces (Fig. 2(d)). The presence of $Ti_3C_2T_x$ flakes in the composite was also confirmed by energy-dispersive X-ray spectroscopy (EDX) mapping (Fig. S3, ESI†). Further characterization of the materials including XPS, FTIR and Raman spectroscopies have been conducted in a previous work that confirmed the presence of OH, O, and F terminals on $Ti_3C_2T_x$ and suggested hydrogen bonding between the hydroxyl groups of alginate and the surface groups of MXene filler.[18]

The apparent density of the foams is around 0.085 g cm^{-3} and the corresponding porosity is 93%, which does not vary significantly with the $Ti_3C_2T_x$ content (Table 1). These unchanged porosity values suggest that $Ti_3C_2T_x$ does not compromise the pore formation and is consistent with other lyophilized $Ti_3C_2T_x$ composite aerogels.[21,23] On the contrary, alginate and $Ti_3C_2T_x$ films have a density and porosity of 1.078 and 2.140 g cm^{-3} and 14 and 48%, respectively. Furthermore, the incorporation of $Ti_3C_2T_x$ enhanced the mechanical properties of the foams as seen from compressive stress–strain curves of alginate and 5%$Ti_3C_2T_x$-alginate foams (Fig. S4, ESI†). The Young's modulus increased from 22.7 ± 4.9 kPa to 25.6 ± 5.2 kPa for the composite foam with a compressive stress of 1.25 MPa at 80% strain.

Foam-based triboelectric nanogenerator

A triboelectric nanogenerator (TENG) was constructed using these foams as the tribopositive component and a mixed cellulose ester film as the tribonegative counterpart (see Fig. 1(b)). The alginate foams with thicknesses of 1.6 and 3 mm generated a peak-to-peak output voltage of around 310 V, while the 6 mm foam produced a lower output of 180 V (Fig. 3(a)). A similar trend was observed for the short-circuit current density (I_{sc}), which decreased from 5.5 mA m^{-2} to 1.9 mA m^{-2} with increasing foam thickness (Fig. 3(b)). For comparison, the voltage and I_{sc} of a non-porous alginate film (0.025 mm thickness) were also measured, delivering 335 V and 9.1 mA m^{-2}, respectively. The observed decrease in voltage and current density with increasing thickness of the tribo-layer can be explained by the DDEF model of triboelectric output.[12,32] Herein, the open-circuit voltage (V_{oc}) and I_{sc} depend inversely on the thickness of the dielectric tribo-layer. The electric field, originating from charges on the contact surface, propagates into the dielectric layer until the dielectric–electrode interface. The field induces a potential and a current flow through the external circuit to balance the potential difference. The further the field travels into the layer, the weaker it becomes, and so do the induced output voltage and current, as shown by experiments and simulations.[12] The DDEF model primarily focuses on dense dielectric layers. However, two key parameters that are often neglected can play a significant role in optimizing TENG output with foams: (i) the relative permittivity, ε_r, which has an inverse relation, and (ii) the contact surface area, which has a direct relation with both V_{oc} and I_{sc} according to the DDEF model. Porous dielectric materials tend to exhibit a lower ε_r value (closer to the value of air) and a higher contact surface than their dense counterpart. Consequently, we expect that the output decay associated with increasing the thickness of a porous layer will not be as drastic as for a thick alginate-dense layer. Studies have demonstrated that the increased surface area of porous and microstructured layers increases the triboelectric output compared to their non-porous forms, as more charges can be stored on the contact surface, according to the output current of a TENG,

$$I = A\frac{d\sigma}{dt}, \quad (2)$$

where A is the surface area, and σ is the charge density.[9,14,15,33] Therefore, the larger surface area (discussed in more detail below) of the foams likely mitigates, to some extent, the output reduction associated with increased layer thickness. This helps explain the relatively low output decay of the 1.6- and 3-mm foams compared to the thin, dense alginate film.

To enhance the triboelectric output of the 6 mm-foams, the amount of $Ti_3C_2T_x$ in the alginate composite was increased, resulting in the voltage increase from 180 V to 385 V for the 5%$Ti_3C_2T_x$-alginate composite (Fig. 3(c)). This clearly shows that incorporating $Ti_3C_2T_x$ overcomes the voltage decay associated with thickness. It can be reasoned that adding MXenes may enhance the surface charge density of the composite foams through hydrogen bond interactions between the T_x (OH, O, F) terminations and the alginate hydroxyl groups, as previously shown for MXene-alginate films using Kelvin probe force microscopy (KPFM).[18] Note that these studies were performed on model films suitable for KPFM, but we deem that the

Table 1 Textural properties of the foams and films for comparison

Conformation	$Ti_3C_2T_x$ (wt%)	Density g cm^{-3}	Porosity %
Film	0	1.078	14
Film	100	2.140	48
Foam	0	0.085	93
Foam	1	0.085	93
Foam	2	0.087	93
Foam	5	0.083	93

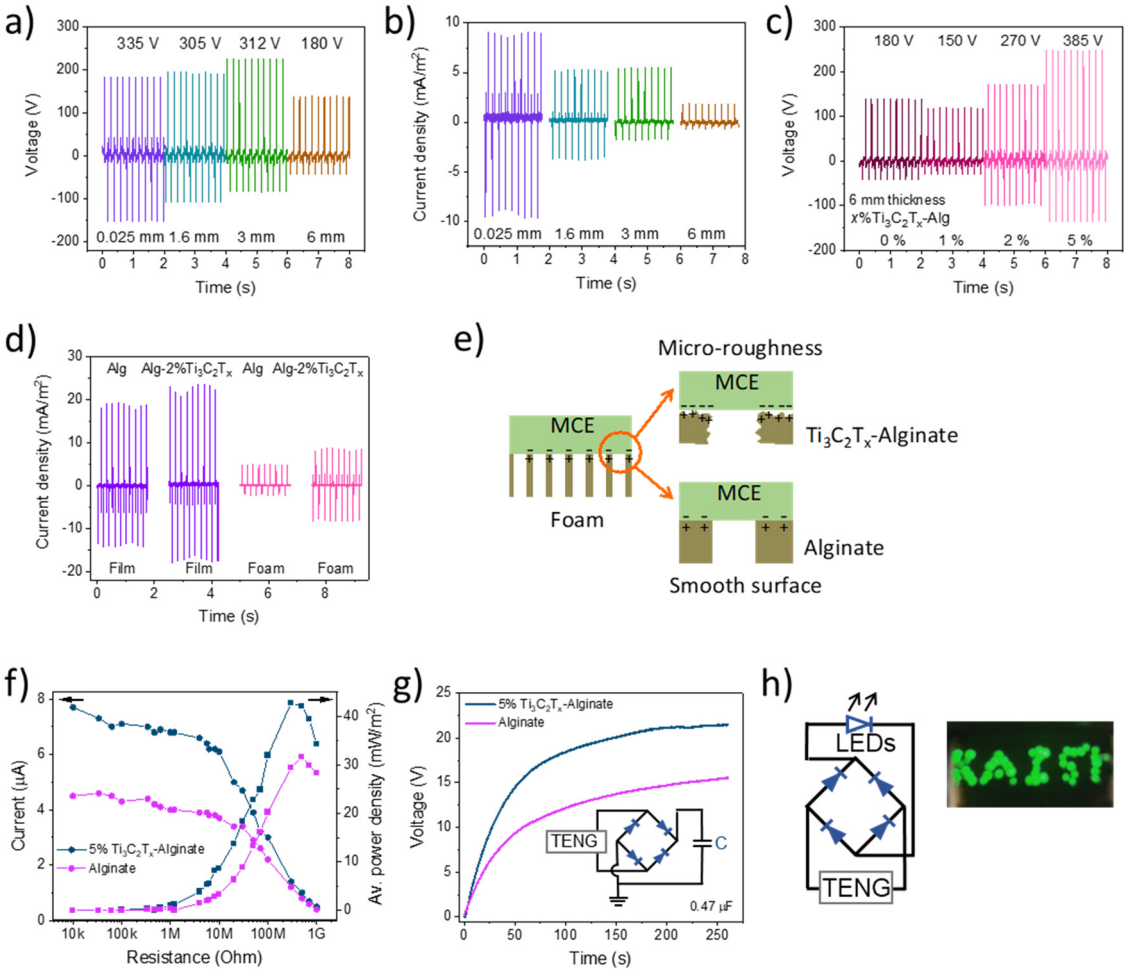

Fig. 3 Triboelectric performance of dense films and porous foams. Triboelectric voltage (a) and current (b) output of an alginate film and alginate foams of different thicknesses. Voltage of 6 mm thick foams with varying wt% of $Ti_3C_2T_x$ (c). The current density of films and 6 mm-foams (d), illustration of the influence of $Ti_3C_2T_x$ on the micro-roughness and charge generation of foam cell walls (e). Short-circuit current and time-averaged power density curves (f), capacitor charging curves (g), and powering LEDs with a 5%$Ti_3C_2T_x$-alginate foam TENG (h).

conclusions can be extrapolated to the present foam samples. Although adding $Ti_3C_2T_x$ to the alginate film only enhanced the current density by 25%, its incorporation into the alginate foam improved the current output by 80%, albeit at lower absolute levels (Fig. 3(d)). This significant increase in output current can be attributed to a larger surface charge density in foams that resulted in higher output values, according to eqn (2). The surface roughness from adding additives and (or) nano/micro-structuring is also known to increase the TENGs performance.[34] Here, the composite foams display a rougher internal surface than their alginate counterparts, as shown in Fig. 2(c) and (d), similar to previous observations of MXene-alginate films.[18] These surface features create friction and enhance the contact surface with the MCE film (Fig. 3(e)), potentially leading to higher triboelectrification and output.[34] The current and time-averaged power density curves clearly show the improved performance of the 5%$Ti_3C_2T_x$-alginate composite foams, which delivered 7.8 μA and 42 mW m^{-2} (Fig. 3(f)). These values are in the range of TENG output reported for centimeter-thick foams of polyurethane (2.2 μA, 5.2 mW m^{-2})[14] or polyaniline (6.3 μA, 172 mW m^{-2})[17] and micrometer-thin aerogels that deliver instantaneous power of 0.1–20 W m^{-2} (Table S1, ESI† for comparison).[10] When a 0.47 μF capacitor was charged, the 5% $Ti_3C_2T_x$ composite foam reached 21 V after 200 s, whereas the alginate foam only delivered 14 V during the same period (Fig. 3(g)). The total generated energy from the composite and alginate foams was 0.1 mJ and 0.05 mJ, respectively. Furthermore, we demonstrated that a TENG constructed with this composite foam can power a 50-LED array connected to a bridge rectifier (Fig. 3(h)).

Thermal insulation behavior of composite foams

To investigate thermal insulation properties, foams were placed on a 50 °C hot plate, and the surface temperature of the foams was determined using a thermographic camera. After 30 minutes, the surface temperature of the alginate foam was 35.5 °C, which increased with the incorporation of $Ti_3C_2T_x$. (Fig. 4(a)). The highest temperature of 39.0 °C was observed at 1% $Ti_3C_2T_x$ content, while the temperature decreased to 36.5 °C for the 5% $Ti_3C_2T_x$ composite foam. The results demonstrate the thermal

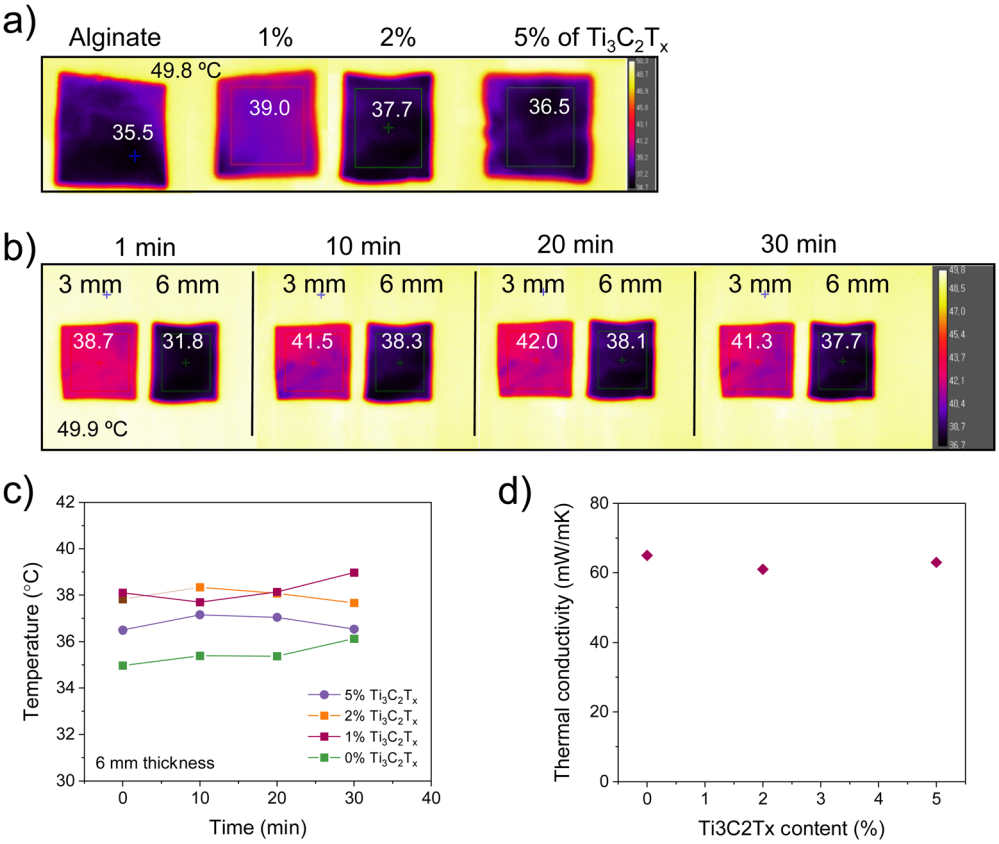

Fig. 4 Thermal insulation behavior of foams. Thermographic camera images of 6 mm thick alginate and $Ti_3C_2T_x$-alginate foams taken after 30 min on a 50 °C-hot plate (a) and of 2%$Ti_3C_2T_x$-alginate foams with different thicknesses (3 and 6 mm) at different times (b), respectively. Evolution of the surface temperature of 6 mm foams with varying $Ti_3C_2T_x$ content (c). Thermal conductivity of $Ti_3C_2T_x$-alginate foams (d) including error bars of 1 and 0 mW k^{-1} m^{-1}.

insulation behavior of the composites, reducing the temperature by approximately 14 °C across the 6 mm foam. The temporal evolution of the surface temperature of 2% $Ti_3C_2T_x$ composite foams of 3 and 6 mm thicknesses was also investigated (Fig. 4(b)). The thicker foam maintained a lower temperature (approximately 38 °C) over time than the thinner foam (approximately 41 °C). Importantly, the surface temperature remained largely constant after 1 minute over the entire observation time, as also recently observed for $Ti_3C_2T_x$ films.[26] This behavior was further studied in 6 mm foams with varying $Ti_3C_2T_x$ content (Fig. 4(c)). The alginate foam has the lowest surface temperature (35 °C), and it increased by 1 °C over 30 min. In contrast, adding 1% $Ti_3C_2T_x$ increased the temperature by 3 °C. With further increasing the $Ti_3C_2T_x$ content to 2 and 5%, the temperatures were lower than that of the 1% $Ti_3C_2T_x$ foam, with the highest temperature recorded at ~10 min.

Moreover, the transient thermal conductivity measurements of the alginate and composite foams show values of 63 and 62 mW m^{-1} K^{-1}, respectively (Fig. 4(d)), which are only a little higher than commercial insulation materials like expanded polystyrene foams (35–45 mW m^{-1} K^{-1}).[35] Altogether, these results suggest that the thermal behavior of the composite foams depends more on the thermal properties of $Ti_3C_2T_x$ than textural changes, as density and porosity remain largely constant across the tested foam compositions (see Table 1).

The thermal properties of MXenes have been recently investigated, and $Ti_3C_2T_x$ was found to display extremely low IR emissivity in the mid-IR range (ε = 0.06), resulting in radiative cooling effects of $Ti_3C_2T_x$ films.[24–26,36] The thermal conductivity of $Ti_3C_2T_x$ films and flakes has also been measured, offering deviating results. While in-plane conductivity values of 2–17 W m^{-1} K^{-1} were determined for films using macroscopic characterization techniques,[37,38] scanning probe measurements on individual, monolayered flakes yielded 0.78 W m^{-1} K^{-1} (in-plane) and 0.38 W m^{-1} K^{-1} (through-plane).[39] From these measurements, a heat conduction mechanism based on phonon transport in the film and electron transport in the flakes was proposed.

In the present case, we may assume that the thermal behavior of the composite foams is influenced by the IR emission and thermal conductivity of $Ti_3C_2T_x$. The lower surface temperature observed at higher $Ti_3C_2T_x$ content is likely attributed to the dominance of the low IR emissivity, hinting at a radiative cooling effect, as more $Ti_3C_2T_x$ sheets are present at the surface. The resulting constant surface temperature below the hot plate temperature suggests a low steady heat transfer rate across the foams, which is essential for thermal insulation materials. The relatively low thermal conductivity of the composite foams could be ascribed to the low conductivity of

$Ti_3C_2T_x$ flakes that do not compromise the thermal insulation behavior of the alginate matrix. Additionally, alginate polymer chains surrounding the flakes likely act as thermal barrier as shown for BN nanosheet–polymer composite films.[40] This is attributed to interfacial phonon scattering that effectively reduces the thermal conductivity of nanostructured composites and nanomaterials.[2,38,41]

Flame retardancy of composite foams

The thermal decomposition of neat alginate and 5% $Ti_3C_2T_x$-alginate was investigated by thermogravimetric (TG) analysis to evaluate whether the inclusion of $Ti_3C_2T_x$ affected the thermal stability of the composites. The TG plots in nitrogen (Fig. S5a, ESI†) show the typical weight loss pattern of sodium alginate with the initial removal of water up to 200 °C, followed by thermal decomposition that leads to the formation of thermally unstable chars. These chars are gradually converted to Na_2O and Na_2CO_3 at temperatures above 800 °C.[42,43] In air, the carbonaceous char produced at lower temperatures oxidized at 610 °C, leading to a final residue mostly comprised of Na_2O and Na_2CO_3 (Fig. S5b, ESI†).[44] The addition of $Ti_3C_2T_x$ did not affect the thermal stability of the alginate matrix when the TG test was conducted in nitrogen. In air, however, the oxidation of char takes place at a temperature of 550 °C and at a slower rate with respect to neat alginate, leading to similar residual mass (*i.e.*, 26%). This behavior may be attributed to the catalytic effect of $Ti_3C_2T_x$ and its calcination product, TiO_2,[45] on the polymer carbonization.[28]

The flame retardant properties of the foams were evaluated through flammability tests, subjecting the materials to a butane torch flame for 28 s (Fig. 5). The aim was to evaluate preliminarily the foam reaction to the exposure of a small flame. The alginate and the 2 and 5% $Ti_3C_2T_x$-alginate composites exhibited flame retardant and self-extinguishing characteristics, as demonstrated by snapshots taken at various intervals. The materials did not continue to burn once the torch was removed and displayed intumescent behavior, *i.e.*, the blowing up of charred material, which was obvious in the case of alginate foam (Fig. 5(a)). Intumescence is generally caused by the generation of gases (*e.g.*, CO_2, CO, H_2O) during pyrolysis[46] and the absence of crosslinking networks in sodium alginate.[42] The addition of $Ti_3C_2T_x$ reduced the extent of intumescence while maintaining the self-extinguishing properties of the foams (Fig. 5(b) and (c)). A possible explanation for the reduced intumescence could be the cross-linking between the MXene flakes and alginate chains, sustained by the strong hydrogen bond interactions, as previously investigated.[18]

The behavior of the foams under a heat flux of 35 kW m^{-2} was analyzed using cone calorimetry tests. Snapshots of the samples during this test and the residues collected afterward are presented in Fig. 6(a) and (b). The alginate foam displays intumescent behavior, as previously observed in the flammability tests. The intumescence ceases after 180 s, producing a

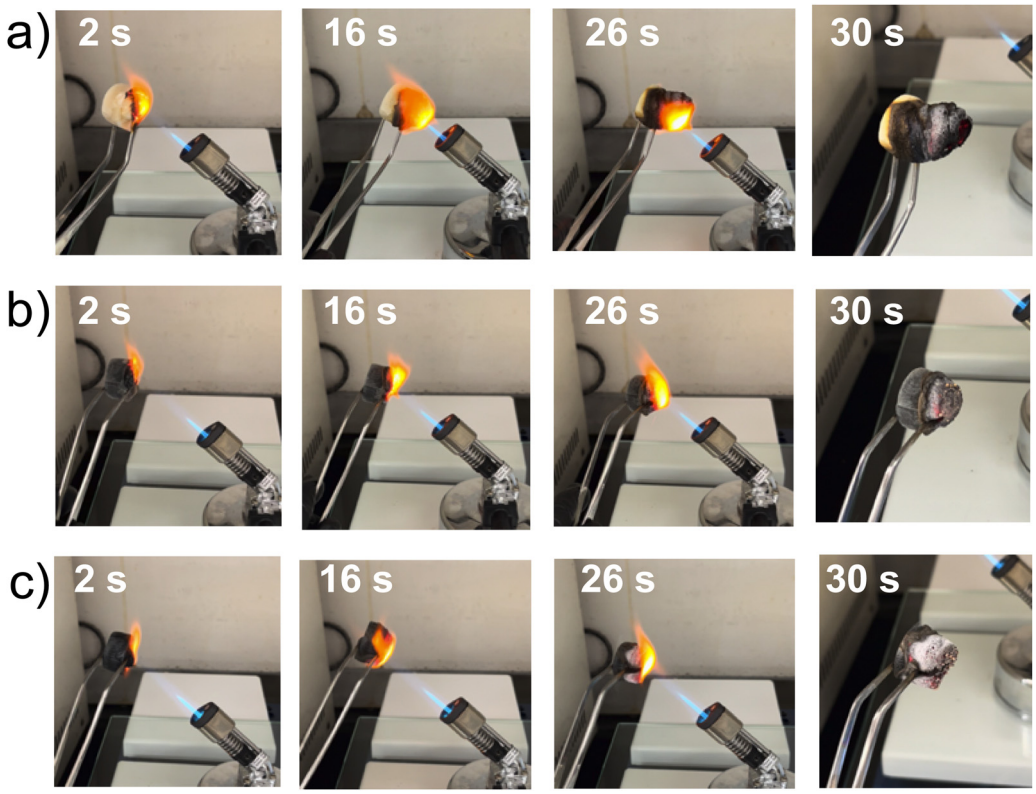

Fig. 5 Flammability test of foams. Alginate (a), 1%$Ti_3C_2T_x$-alginate (b), and 5%$Ti_3C_2T_x$-alginate (c) foams subjected to a butane torch flame; snapshots were taken after 2, 16, 26, and 30 s.

foamed and charred residue three times its initial height (Fig. 6(a)). No ignition was observed during the entire 500 s test, further supported by the extremely low heat release rate (HRR) values (Fig. S6, ESI†). This suggests that the concentration of the volatiles remained below the lower flammability limit. The residue collected at the end of the test accounted for 33% of the initial mass and showed a charred, brittle structure with macroscopic pores (Fig. 6(b)). The 5% $Ti_3C_2T_x$ composite foams also showed non-igniting behavior. In contrast to the pure alginate foams, these samples did not exhibit intumescence and partially shrank during exposure to the cone heat flux. This shrinkage may be related to the extensive hydrogen bonding between $Ti_3C_2T_x$ and the alginate, which restricts the mobility of the polymer chains and inhibits their ability to intumesce.[18] The final residues of this composite accounted for 26% of the initial mass and had a greyish color. This observation, coupled with the final residue from the TG analysis in air and the higher HRR values (Fig. S6, ESI†), suggests the occurrence of extensive oxidation reactions in the condensed phase of the $Ti_3C_2T_x$ composite during the cone test. The absence of intumescence may have prevented the formation of a barrier that limits heat and mass transfer.[46] Investigations on post-combustion residues using XRD (Fig. 6(c)) and SEM/EDX (Fig. S7, ESI†) corroborate this theory. Both alginate and $Ti_3C_2T_x$-alginate residues were found to contain sodium, oxygen, and carbon. The former had a relatively high carbon content, while the latter residue showed limited carbon content.[44] Additionally, titanium was detected in this residue, attributed to the oxidation of $Ti_3C_2T_x$ to TiO_2.[45] This is in stark contrast to the XRD pattern of the composite before combustion showing only the shoulder of the (002) reflection of $Ti_3C_2T_x$ besides the amorphous halo of alginate (Fig. S8, ESI†).

$Ti_3C_2T_x$-alginate based smart fire alarm system

The thermoresistive properties of the $Ti_3C_2T_x$-alginate foams were studied to design a fire alarm system based on changes in electrical resistance. A 5%$Ti_3C_2T_x$ composite foam was connected to wires to measure the electrical resistance across a rectangular slab when exposed to heat (Fig. 7(a)). When the composite was heated to 200 °C, the resistance decreased from 2500 to 1000 Ohms, then increased to 1200 Ohms during the subsequent isothermal stage. This initial decrease in resistance is likely due to the dehydration and shrinkage of the material. Thermal analysis indicated a weight loss of about 9% up to

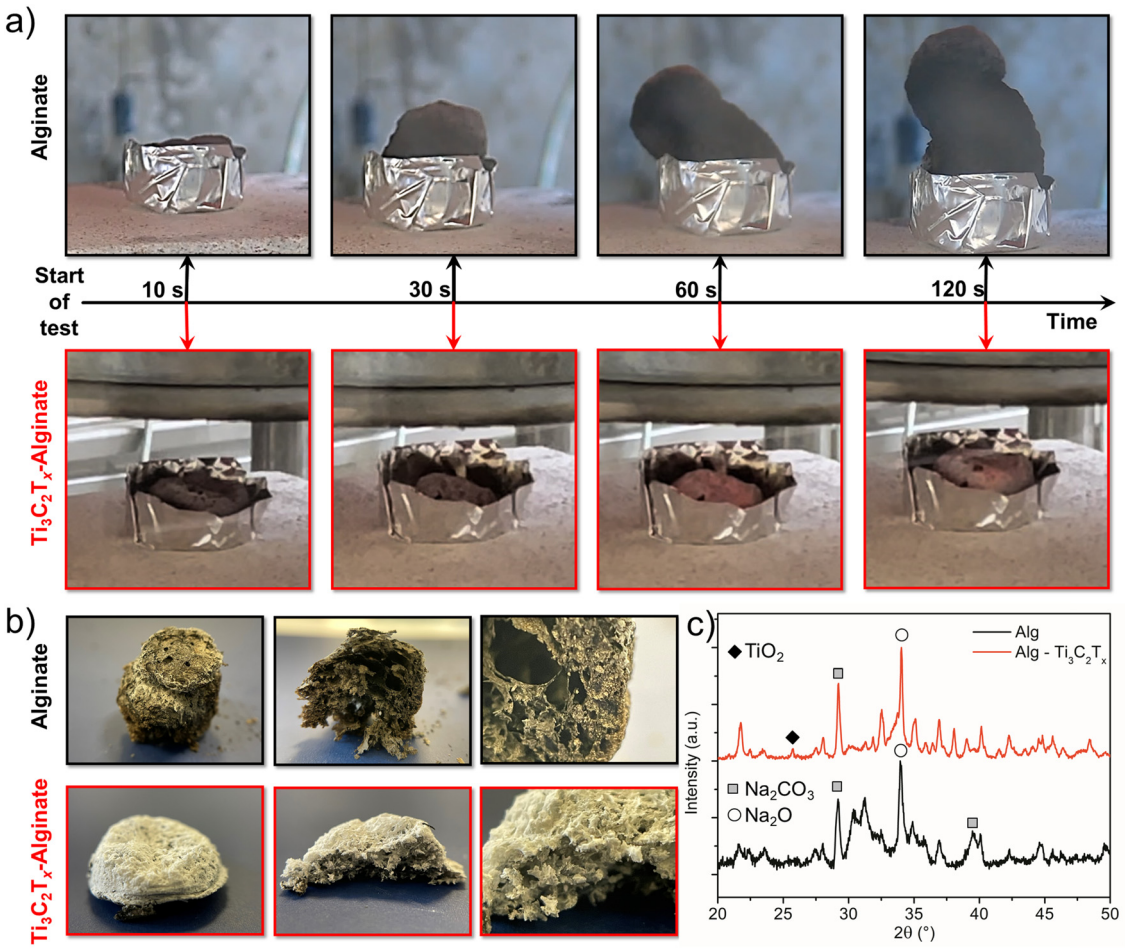

Fig. 6 Cone calorimetry tests of foams. Digital images of the foams during the tests (a) and after collecting the residues (b). XRD diffractograms of the residues of alginate and 5%$Ti_3C_2T_x$-alginate (c).

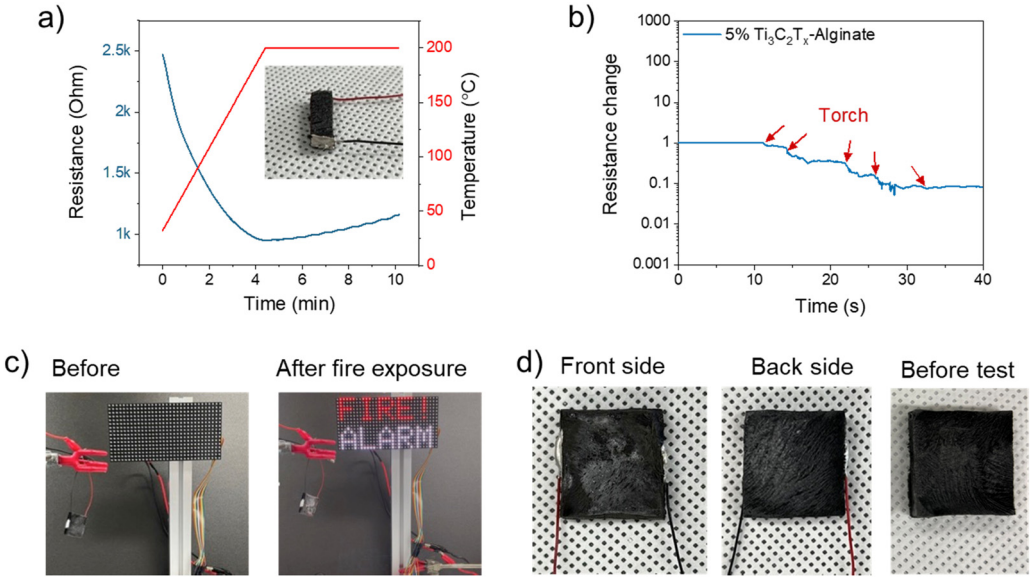

Fig. 7 Electrical behavior and smart fire alarm demonstration. The electrical resistance of a 5%$Ti_3C_2T_x$-alginate foam (inset photo showing the wired foam slab) during heating (a) and when exposed multiple times to a torch flame, indicated by the red arrows (b). Photographs showing an electric panel before and after fire exposure of a 5%$Ti_3C_2T_x$-alginate foam, with a fire alarm message appearing within 2 s of fire exposure(c). Photographs showing the front and backside of the foam after fire exposure as well as before the test (d).

200 °C (Fig. S5, ESI†), which can be attributed to the removal of physisorbed water. Both alginate and $Ti_3C_2T_x$ are hygroscopic materials that adsorb moisture from the ambient atmosphere. Removing this water from the foam enhances the electrical conductivity of the foam walls, as the adsorbed water previously acted as an insulating layer. Additionally, the concomitant shrinkage of the foam likely increases the connectivity between the foam walls and the $Ti_3C_2T_x$ flakes, thereby increasing the number of conduction paths within the foam. The resistance changes of the foam were also monitored during exposure to a torch flame (Fig. S9, ESI†). The resistance dropped each time the flame impinged on the sample (red arrows in Fig. 7(b)), resulting from water removal, pore shrinkage, and localized polymer carbonization. The latter contributes to forming a conductive C/N-doped TiO_2 network resulting from the oxidation of $Ti_3C_2T_x$, as suggested by Mao *et al.*[47] These relative changes in resistance can be used to activate an LED display connected to a programmable controller unit (Fig. S10, ESI†). The electrical trigger threshold was set to a 10% change in resistance, and a fire alarm was activated just 2 s after the foam was exposed to the torch flame (Fig. 7(c) and Video S1, ESI†). Quick alarm response times are crucial for ensuring safety and minimizing material and human damage in the event of a fire hazard. In comparison, other MXene-based polymer composites have triggered fire alarm after 1 to 20 seconds.[47,48] Upon examining the foam after the test, it was observed that the front side, where the flame contacted the sample, showed only minimal signs of combustion damage, while the back side remained undamaged (Fig. 7(d)). For comparison, Fig. 7(d) also shows the foam surface before the test and confirms the insignificant damage. This implies that the material has high burn-through resistance similar to that of polysaccharide-clay foams,[49] indicating that the short exposures to fire do not compromise the integrity of the material, which is important for reuse. In fact, the material remains operational for further alarms, which can also be seen from the repeated resistance drops in Fig. 7(b).

Conclusions

We have demonstrated that composite foams made from $Ti_3C_2T_x$ and alginate possess multifunctional and complementary properties. Incorporating $Ti_3C_2T_x$ allowed millimeter-thick foams to be used in TENG devices, which would not be possible otherwise. The increased thickness enhances the triboelectric output to 380 V, 7.7 μA and 43 mW m^{-2} while also providing thermal insulation. The composite foam panels have a very low thermal conductivity of 62 mW m^{-1} K^{-1}. Additionally, these composite foams displayed flame-retardant properties. Furthermore, our findings revealed that the electrical resistance of the foams decreased upon fire exposure, which forms the basis for designing a fast-response fire alarm system capable of triggering a warning signal in just 2 seconds. The versatility of the $Ti_3C_2T_x$-alginate foams may lead to a new generation of smart insulation materials that conserve energy in the built environments, generate electricity through the triboelectric effect, and serve as an effective flame-retardant and fire alarm system.

Author contributions

Bernd Wicklein: investigation, data curation, conceptualization, funding acquisition, writing – original draft. Hyunjoon Yoo: investigation, methodology, writing – review & editing.

Geetha Valurouthu: investigation, data curation, writing – review & editing. Ji-Seok Kim: methodology, validation. Mannan Khan: methodology. Manmatha Mahato: formal analysis. Federico Carosio: investigation, formal analysis, writing – review & editing. Yury Gogotsi: supervision, validation, writing – review & editing. Il-Kwon Oh: conceptualization, supervision, writing – review & editing.

Data availability

The data supporting this article have been included as part of the ESI.†

Conflicts of interest

There are no conflicts to declare.

Acknowledgements

This work was supported by the National Research Foundation of Korea (NRF) grant funded by the Korean government (MSIT) (2022H1D3A2A01082141). BW acknowledges the grants PID2019-107022RJ-I00 and RYC2021-034164-I, funded by MCIN/AEI/10.13039/501100011033 and by the "European Union NextGenerationEU/PRTR". YG acknowledges The Charles T. and Ruth M. Bach Endowment, Drexel University.

References

1 C. Wang, Y. Zhang, B. Zhang and J. Yang, *Adv. Funct. Mater.*, 2023, **33**, 2205537.
2 B. Wicklein, A. Kocjan, G. Salazar-Alvarez, F. Carosio, G. Camino, M. Antonietti and L. Bergström, *Nat. Nanotechnol.*, 2015, **10**, 277–283.
3 *Springer Handbook of Aerogels*, ed. M. A. Aegerter, N. Leventis, M. Koebel, and S. A. Steiner III, Springer, Cham, 1st edn, 2023.
4 S. J. Yeo, M. J. Oh and P. J. Yoo, *Adv. Mater.*, 2019, **31**, 1803670.
5 N. Wu, Y. Yang, C. Wang, Q. Wu, F. Pan, R. Zhang, J. Liu and Z. Zeng, *Adv. Mater.*, 2023, **35**, 2207969.
6 R. Banerjee, A. Gebrekrstos, J. T. Orasugh and S. S. Ray, *Ind. Eng. Chem. Res.*, 2023, **62**, 6807–6842.
7 U. G. K. Wegst, P. H. Kamm, K. Yin and F. García-Moreno, *Nat. Rev. Methods Primers*, 2024, **4**, 28.
8 M.-A. Shahbazi, M. Ghalkhani and H. Maleki, *Adv. Eng. Mater.*, 2020, **22**, 2000033.
9 Q. Zheng, L. Fang, H. Guo, K. Yang, Z. Cai, M. A. B. Meador and S. Gong, *Adv. Funct. Mater.*, 2018, **28**, 1706365.
10 M. M. Rastegardoost, O. A. Tafreshi, Z. Saadatnia, S. Ghaffari-Mosanenzadeh, C. B. Park and H. E. Naguib, *Nano Energy*, 2023, **111**, 108365.
11 C. Wu, A. C. Wang, W. Ding, H. Guo and Z. L. Wang, *Adv. Energy Mater.*, 2019, **9**, 1802906.
12 R. D. I. G. Dharmasena, K. D. G. I. Jayawardena, C. A. Mills, J. H. B. Deane, J. V. Anguita, R. A. Dorey and S. R. P. Silva, *Energy Environ. Sci.*, 2017, **10**, 1801–1811.
13 X. Kang, C. Pan, Y. Chen and X. Pu, *RSC Adv.*, 2020, **10**, 17752–17759.
14 H. Zhang, Y. Lu, A. Ghaffarinejad and P. Basset, *Nano Energy*, 2018, **51**, 10–18.
15 Z. Haider, A. Haleem, R. u S. Ahmad, U. Farooq, L. Shi, U. P. Claver, K. Memon, A. Fareed, I. Khan, M. K. Mbogba, S. M. C. Hossain, F. Farooq, W. Ali, M. Abid, A. Qadir, W. He, J. Luo and G. Zhao, *Nano Energy*, 2020, **68**, 104294.
16 Z. Saadatnia, S. G. Mosanenzadeh, E. Esmailzadeh and H. E. Naguib, *Sci. Rep.*, 2019, **9**, 1370.
17 Y. Liu, Y. Zheng, Z. Wu, L. Zhang, W. Sun, T. Li, D. Wang and F. Zhou, *Nano Energy*, 2021, **79**, 105422.
18 B. Wicklein, G. Valurouthu, H. Yoon, H. Yoo, S. Ponnan, M. Mahato, J. Kim, S. S. Ali, J. Y. Park, Y. Gogotsi and I.-K. Oh, *ACS Appl. Mater. Interfaces*, 2024, **16**, 23948–23959.
19 A. VahidMohammadi, J. Rosen and Y. Gogotsi, *Science*, 2021, **372**, eabf1581.
20 Y. Dong, S. S. K. Mallineni, K. Maleski, H. Behlow, V. N. Mochalin, A. M. Rao, Y. Gogotsi and R. Podila, *Nano Energy*, 2018, **44**, 103–110.
21 Z. Zhou, J. Liu, X. Zhang, D. Tian, Z. Zhan and C. Lu, *Adv. Mater. Interfaces*, 2019, **6**, 1802040.
22 S. Zhao, H.-B. Zhang, J.-Q. Luo, Q.-W. Wang, B. Xu, S. Hong and Z.-Z. Yu, *ACS Nano*, 2018, **12**, 11193–11202.
23 M. Han, X. Yin, K. Hantanasirisakul, X. Li, A. Iqbal, C. B. Hatter, B. Anasori, C. M. Koo, T. Torita, Y. Soda, L. Zhang, L. Cheng and Y. Gogotsi, *Adv. Opt. Mater.*, 2019, **7**, 1900267.
24 Y. Li, C. Xiong, H. Huang, X. Peng, D. Mei, M. Li, G. Liu, M. Wu, T. Zhao and B. Huang, *Adv. Mater.*, 2021, **33**, 2103054.
25 C. Wen, B. Zhao, Y. Liu, C. Xu, Y. Wu, Y. Cheng, J. Liu, Y. Liu, Y. Yang, H. Pan, J. Zhang, L. Wu and R. Che, *Adv. Funct. Mater.*, 2023, **33**, 2214223.
26 M. Han, D. Zhang, A. Singh, T. Hryhorchuk, C. Eugene Shuck, T. Zhang, L. Bi, B. McBride, V. B. Shenoy and Y. Gogotsi, *Mater. Today*, 2023, **64**, 31–39.
27 L. Zhao, L. Bi, J. Hu, G. Gao, D. Zhang, Y. Li, A. Flynn, T. Zhang, R. Wang, X. M. Cheng, L. Liu, Y. Gogotsi and B. Li, *Nat. Commun.*, 2024, **15**, 10027.
28 L. Liu, J. Feng, Y. Xue, V. Chevali, Y. Zhang, Y. Shi, L.-C. Tang and P. Song, *Adv. Funct. Mater.*, 2023, **33**, 2212124.
29 W. Chen, P. Liu, Y. Liu and Z. Liu, *Chem. Eng. J.*, 2022, **446**, 137239.
30 T. S. Mathis, K. Maleski, A. Goad, A. Sarycheva, M. Anayee, A. C. Foucher, K. Hantanasirisakul, C. E. Shuck, E. A. Stach and Y. Gogotsi, *ACS Nano*, 2021, **15**, 6420–6429.
31 S. Deville, *Adv. Eng. Mater.*, 2008, **10**, 155–169.
32 H. Zhang, L. Yao, L. Quan and X. Zheng, *Nanotechnol. Rev.*, 2020, **9**, 610–625.
33 Z. L. Wang, *Mater. Today*, 2017, **20**, 74–82.
34 L. Wu, P. Xue, S. Fang, M. Gao, X. Yan, H. Jiang, Y. Liu, H. Wang, H. Liu and B. Cheng, *Mater. Horiz.*, 2024, **11**, 341–362.

35 B. P. Jelle, *Energy Build.*, 2011, **43**, 2549–2563.
36 X. Li, M. Li, X. Li, X. Fan and C. Zhi, *Research*, 2022, **2022**, 9892628.
37 E. Jiao, K. Wu, Y. Liu, M. Lu, Z. Hu, B. Chen, J. Shi and M. Lu, *Composites, Part A*, 2021, **146**, 106417.
38 L. Chen, X. Shi, N. Yu, X. Zhang, X. Du and J. Lin, *Materials*, 2018, **11**, 1701.
39 Y. Huang, J. Spiece, T. Parker, A. Lee, Y. Gogotsi and P. Gehring, *ACS Nano*, 2024, **18**, 32491–32497.
40 Y. Wu, Y. Xue, S. Qin, D. Liu, X. Wang, X. Hu, J. Li, X. Wang, Y. Bando, D. Golberg, Y. Chen, Y. Gogotsi and W. Lei, *ACS Appl. Mater. Interfaces*, 2017, **9**, 43163–43170.
41 X. Qian, J. Zhou and G. Chen, *Nat. Mater.*, 2021, **20**, 1188–1202.
42 Y.-J. Xu, L.-Y. Qu, Y. Liu and P. Zhu, *Carbohydr. Polym.*, 2021, **260**, 117827.
43 A. B. Ross, C. Hall, K. Anastasakis, A. Westwood, J. M. Jones and R. J. Crewe, *J. Anal. Appl. Pyrolysis*, 2011, **91**, 344–351.
44 P. dos Santos Araújo, G. B. Belini, G. P. Mambrini, F. M. Yamaji and W. R. Waldman, *Int. J. Biol. Macromol.*, 2019, **140**, 749–760.
45 M. Naguib, O. Mashtalir, M. R. Lukatskaya, B. Dyatkin, C. Zhang, V. Presser, Y. Gogotsi and M. W. Barsoum, *Chem. Commun.*, 2014, **50**, 7420–7423.
46 J. Alongi, Z. Han and S. Bourbigot, *Prog. Polym. Sci.*, 2015, **51**, 28–73.
47 M. Mao, K.-X. Yu, C.-F. Cao, L.-X. Gong, G.-D. Zhang, L. Zhao, P. Song, J.-F. Gao and L.-C. Tang, *Chem. Eng. J.*, 2022, **427**, 131615.
48 B. Wang, X. Lai, H. Li, C. Jiang, J. Gao and X. Zeng, *ACS Appl. Mater. Interfaces*, 2021, **13**, 23020–23029.
49 M. Ghanadpour, B. Wicklein, F. Carosio and L. Wågberg, *Nanoscale*, 2018, **10**, 4085–4095.